Bathymetry constrains ocean heat supply to Greenland's largest glacier tongue

Janin Schaffer [1*], Torsten Kanzow [1,2], Wilken-Jon von Appen [1], Luisa von Albedyll [1], Jan Erik Arndt[1] and David H. Roberts[3]

Mass loss from the Greenland ice sheet has increased over the past two decades, currently accounting for 25% of global sea-level rise. This is due to increased surface melt driven by atmospheric warming and the retreat and acceleration of marine-terminating glaciers forced by oceanic heat transport. We use ship-based profiles, bathymetric data and moored time series from 2016 to 2017 of temperature, salinity and water velocity collected in front of the floating tongue of the 79 North Glacier in Northeast Greenland. These observations indicate that a year-round bottom-intensified inflow of warm Atlantic Water through a narrow channel is constrained by a sill. The associated heat transport leads to a mean melt rate of $10.4 \pm 3.1\,\mathrm{m\,yr^{-1}}$ on the bottom of the floating glacier tongue. The interface height between warm Atlantic Water and colder overlying water above the sill controls the ocean heat transport's temporal variability. Historical hydrographic data show that the interface height has risen over the past two decades, implying an increase in the basal melt rate. Additional temperature profiles at the neighbouring Zachariæ Isstrøm suggest that ocean heat transport here is similarly controlled by a near-glacier sill. We conclude that near-glacier, sill-controlled ocean heat transport plays a crucial role for glacier stability.

In the past two decades, the Greenland ice sheet (GrIS) has been losing mass at an accelerated rate, thereby contributing increasingly to global sea-level rise[1–4]. The two major drivers attributed to the mass loss are increased surface melt caused by atmospheric warming and an increased ice discharge due to the speed-up of marine-terminating glaciers and ice streams[5–8]. Oceanic heat fluxes causing increased submarine melting have been shown to be a dominant driver for the glaciers' speed-up and retreat[9–14].

In northern Greenland, the Northeast Greenland ice stream (NEGIS; Fig. 1a) contributes greatly to mass loss of the GrIS, draining 16% of the entire ice sheet[15]. An increased mass loss is predicted in the near future due to an accelerated ice discharge at its main outlet glaciers, Nioghalvfjerdsfjorden Glacier (also referred to as 79 North Glacier (79NG)) and Zachariæ Isstrøm (ZI)[16–18]. Recent studies revealed the loss of the entire glacier tongue and retreat of ZI[16], and ongoing thinning of the 79NG[16,19], with the mass loss of both glaciers having occurred mainly due to increased submarine melting[20]. A reduced buttressing of the glacier flow and grounding-line retreat along a reverse slope may also contribute to destabilization of the glaciers and an increased ice discharge via the NEGIS[21] in the near future.

For the moment, the 79NG possesses the largest floating tongue (Fig. 1c) around the entire coast of Greenland. The glacier's main calving front extends over 35 km and is pinned onto a number of small islands (Fig. 1d). The adjacent bay is covered by fast ice most of the year, which since 2000 has been breaking up more regularly in summer than in previous years[22]. Below a surface layer of polar waters, hydrographic measurements showed the presence of Atlantic Intermediate Water (AIW) in the trough system on the wide continental shelf[23,24] of Northeast Greenland (Fig. 1a,b) and within the cavity below the 80-km-long floating tongue of the 79NG[25–27]. AIW originates from recirculating waters in Fram Strait[23,28] and exceeds 1 °C (Fig. 1b). This makes it more than 3 °C warmer than the in situ freezing point of seawater at 600 m depth (the grounding-line depth

of the 79NG[25]). Using both time-series measurements of the AIW circulation obtained between August 2016 and September 2017 and a survey of the complex bathymetry in the vicinity of the 79NG, we can directly constrain the hitherto unknown dynamics of oceanic heat transport towards the 79NG and its magnitude and variability.

Cavity–shelf exchange flow at the 79NG

In summer 2016, the first multibeam bathymetric survey (Methods) was carried out in front of the 79NG (Fig. 1d). Three gateways between the pinning points were detected to be deep enough to allow for the inflow of warm AIW into the cavity. In particular, we identified a 480-m-deep and 2-km-wide channel leading into the subglacial cavity (site C in Figs. 1d and 2a), while the other two gateways reached 300 m (sites A, B). Bathymetric survey further revealed a 325-m-deep sill that separates the 480-m-deep channel from the trough system on the continental shelf[29] (Figs. 1d and 2c).

To study the exchange of shelf and cavity waters, we (1) collected ship-lowered hydrographic and velocity measurements along the calving front in August 2016 and September 2017 (Methods) and (2) recorded moored hydrographic and velocity time series between August 2016 and September 2017 (Methods and Supplementary Table 1). Moorings were placed at gateways A, B, and C along the main calving front, and at the 130-m-deep sill of Dijmphna Sund (D) connecting the northern, minor calving front of the glacier to the shelf of Northeast Greenland (Fig. 1c,d; velocity recordings at site D stopped in March 2017). Both moored and lowered acoustic Doppler current profiler (ADCP) measurements revealed a swift flow of AIW (waters denser than 27.8 kg m⁻³) reaching 30 to 60 cm s⁻¹ below 400 m depth directed towards the cavity in channel C (Figs. 1d and 2a). At shallower depths (in a layer between 250 m and the glacier front base, located at 90 m), we observed a flow directed out of the cavity showing velocities of up to 20 cm s⁻¹ (Fig. 2a). The outflowing, glacially modified waters are 0.9 °C cooler than the inflowing AIW (Fig. 2b), which suggests cooling from

[1]Alfred Wegener Institute, Helmholtz Centre for Polar and Marine Research, Bremerhaven, Germany. [2]University of Bremen, Bremen, Germany. [3]Department of Geography, Durham University, Durham, UK. *e-mail: janin.schaffer@awi.de
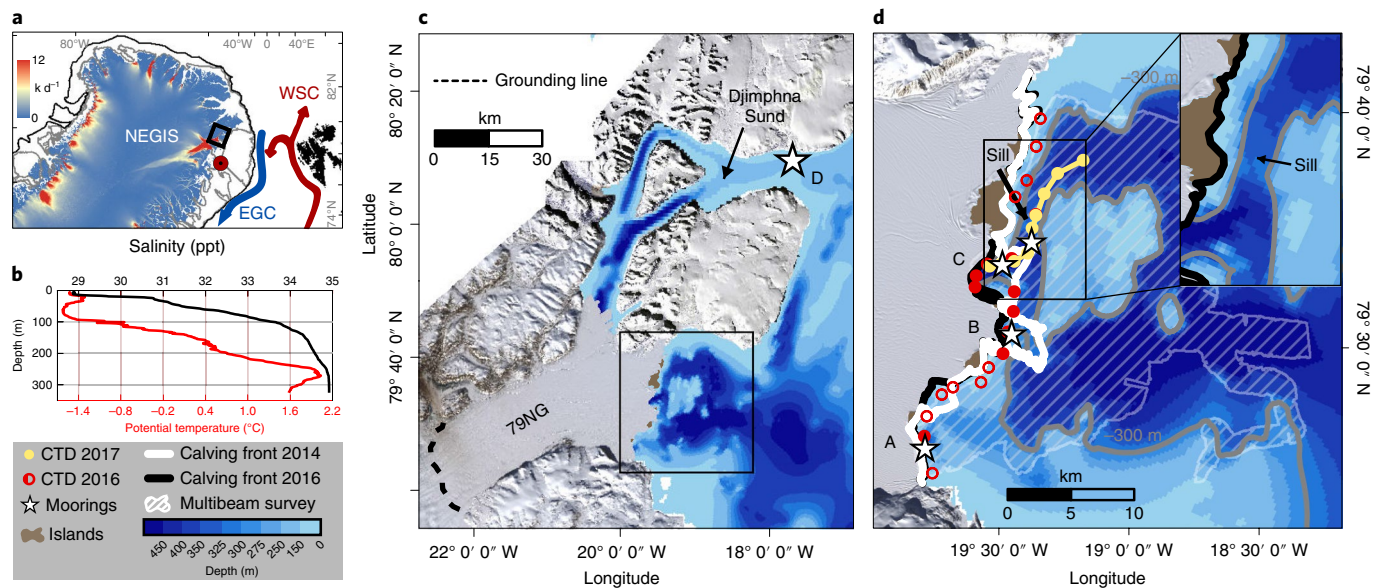
Fig. 1 | Circulation and bathymetry around Northeast Greenland and summer 2016/2017 surveys along the 79NG calving front. a, Map of Greenland with ice velocities and currents sketched around Northeast Greenland and overlaid on the continental shelf bathymetry (300/600 m contours in grey/ black). **b,** Example of a temperature/salinity–depth profile (location marked in **a**) showing typical water properties measured on the continental shelf in summer 2017. **c,** Landsat mosaic of the 79NG and bathymetry of the adjacent ocean (box in **a**). **d,** Enlargement of the 79NG calving front (box in **c**) showing CTD/LADCP stations occupied in 2016 (red, Fig. 2a) and 2017 (yellow, Fig. 2c) and mooring positions (white stars). The close-up in the upper right shows the bathymetric detail of the sill region.

ocean–glacier interaction. The AIW-related heat transport provides a means for basal melting which, by mixing with glacial meltwater within the cavity, transforms dense AIW into cooler, fresher and therefore less-dense waters (modified AIW, referred to as mAIW).

Mean transports integrated horizontally and vertically along the gateways (Methods) reveal that the inflow of AIW is balanced by an outflow of mAIW above 250 m (or densities less than 27.75 kg m^{-3}) (Fig. 2b). The outflow of mAIW through Dijmphna Sound accounts for almost half (45%) of the total export, with the gateways B and C accounting for most of the remaining mAIW outflow. Our moored measurements allow us to calculate a mean (cavity) overturning rate of 46 ± 11 mSv (Fig. 2b; Methods). The total freshwater flux, $Q_{FW} = 0.63 \pm 0.21$ mSv (that is, the sum of subglacial runoff discharged at the grounding line and basal melt), contributes 1.4% to the cavity overturning (Methods). Furthermore, our measurements suggest that considering the time average, most freshwater leaving the cavity originates from basal melting (with a meltwater flux of $Q_{MW} = 0.56 \pm 0.17$ mSv) while only 11% stems from subglacial runoff (Methods). On the basis of our best estimate overturning rate, the average residence time of waters in the cavity is 162 days (Methods), suggesting the glacier to be mostly sensitive to AIW variations on periods longer than half a year[30]. Using our extrapolated temperature time series from moored recorders, the associated annual mean heat transport is 214 ± 6 GW (Methods). Considering the full mass and heat budgets of the subglacial cavity, we find that 97% of the 214 GW of net ocean heat flux into the cavity (H_x) is extracted within the cavity by melting (and warming) the glacier base ($H_{Melting}$; Methods). This leads to area-averaged melt rates of 10.4 ± 3.1 m yr^{-1} (calculated on the basis of the ocean mass, heat and salt budgets alone), translating to 17.8 ± 5.2 km^3 yr^{-1} (note that melt rates near the grounding line are much larger). Our results compare well with estimates derived from glacier mass budget calculations[25], satellite-derived submarine melt rates[20] and melt rates inferred from a plume model[19]. Warmer temperatures observed between January and September 2017 (that is, longer than the residence time) suggest a greater melting response[30] in 2017 compared with autumn 2016 (Fig. 3a).

Sill control of the ocean heat supply

Next, we investigate the dynamics related to the differing (spatial) oceanic characteristics upstream and downstream of the 325-m-deep sill located 4 km upstream of the main inflow channel C (Fig. 1d). We find a bottom-intensified flow at densities exceeding 27.82 kg m^{-3} across the sill that accelerates downstream of the sill towards the cavity (Fig. 2c). Froude numbers (Methods) show a subcritical to supercritical transition across the sill (Fig. 2c) indicative of a hydraulically controlled flow regime in which the density contrast between the cavity and the continental shelf determines the volume flux into the cavity. Hydraulic control theory implies that an increase in the density or height of the AIW upstream of the sill should result in an increased cross-sill flow of AIW, resulting in an increased overturning and heat transport into the cavity.

Time series of hydrographic and velocity records show that the rapid inflow of warm AIW into the cavity is a persistent feature throughout the year (Fig. 3a). This lends support to the conclusion that the AIW flow into the cavity is determined by upstream (hydraulic) control rather than the subglacial discharge at the grounding line of the cavity as the latter is thought to vary greatly between the seasons[13]. Estimated AIW transport from hydraulic control theory based solely on the density (here set mainly by temperature) contrast upstream and downstream of the sill (using moored records from mooring positions A, C and E; Fig. 1d and Methods) explains 59% of the variance of the overturning estimated on the basis of moored velocity measurements (Fig. 3b). In the meantime, using the transport predicted on the basis of hydraulic control theory, we underestimate the calculated overturning by 12%. Furthermore, vertical displacement of the 1.2 °C isotherm upstream of the sill explains 62% of the (measured) overturning variance (with density variations set mainly by temperature variations). We conclude that the sill–channel system in front of the calving front critically controls the oceanic heat supply into the cavity and thereby the melt at the glacier base. The thickness of the AIW layer at the sill (blue line in Fig. 3b) is a crucially important parameter because a thickening corresponds to an increase in the overturning and heat
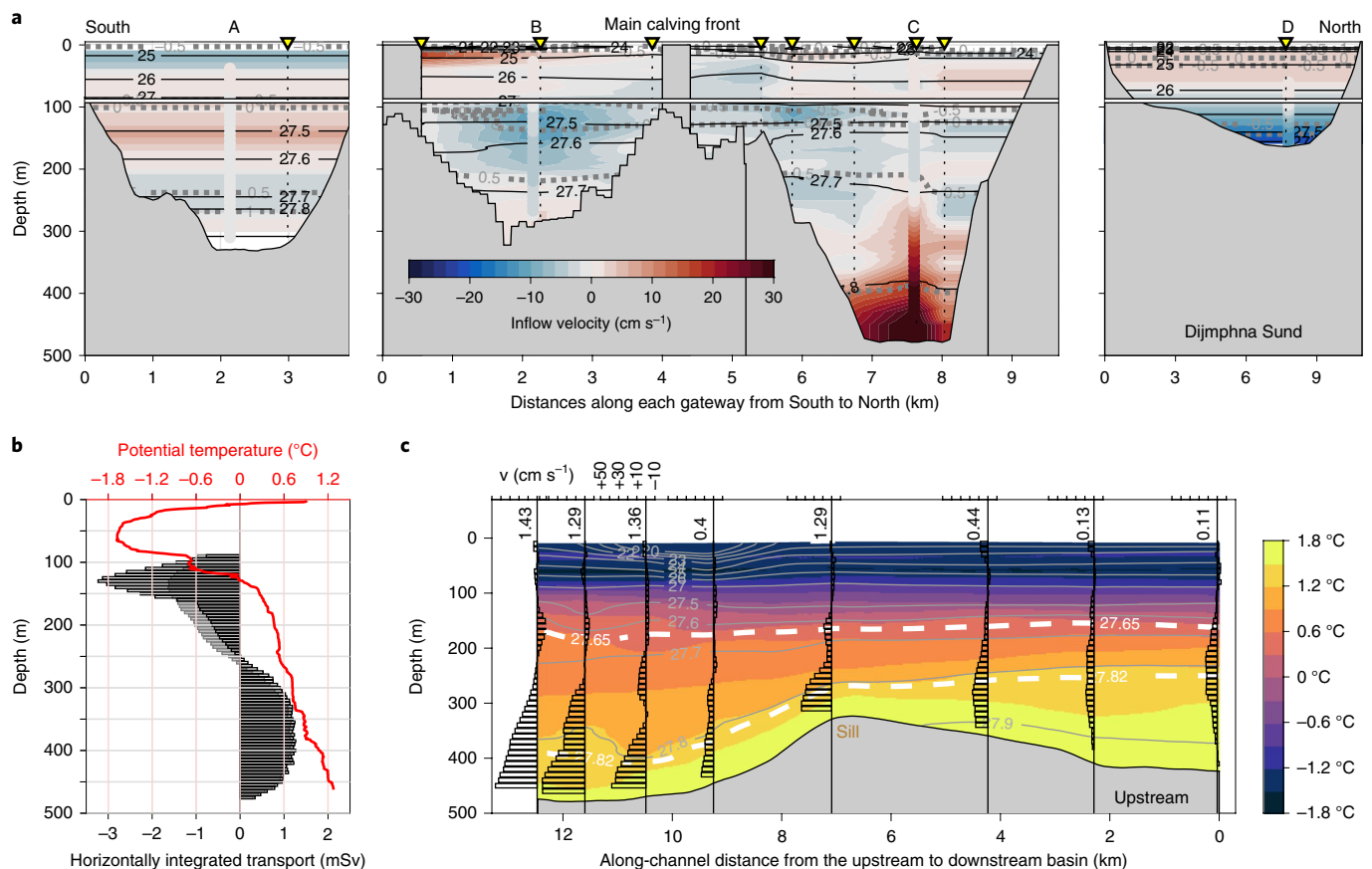
Fig. 2 | Oceanic measurements at the 79NG calving front in 2016/2017. a, Velocity distribution along the 79NG calving front. We marked isopycnals (black), isotherms (grey dashed), station locations (triangles) and the approximate depths of the glacier face (white). At mooring positions A–D, mean velocities from the moored records are overlaid. **b**, Horizontally integrated transports along the calving front section taking Dijmphna Sund into account (black–white) and neglecting Dijmphna Sund records (black–grey), and temperature profile from the main inflow (red). **c**, Potential temperature distribution along the yellow transect in Fig. 1d. Along-channel velocities (bars), 27.65 and 27.82 kg m⁻³ isopycnals (white dashed) and Froude numbers (given at the top of each station) are overlaid.

supplied to melting of the glacier base. Accordingly, our moored records suggest a drastic change in the heat supply occurring in winter 2016/2017, which we link to a large-scale thickening of the AIW layer on the continental shelf (Supplementary Discussion 1 and Supplementary Methods 1).

### Impact of large-scale hydrographic changes

Considering that the moored time series cover the period of one year only, potential processes causing changes on seasonal and longer time scales (which are relevant with respect to a residence time of 162 d) in the AIW height cannot be examined. However, our new knowledge of the local topographic control of AIW inflow can serve to estimate how observed large-scale changes of AIW characteristics on the Northeast Greenland shelf may have affected the basal melting of the 79NG in the recent past. Hydrographic measurements taken some 250 km upstream of the 79NG in the AIW supply pathway from the shelf edge to the 79NG[28] suggest that the AIW layer was 15 m thinner and 0.4 °C cooler in 1984, 1997 and 2008 compared with 2013–2017 (Supplementary Methods 2 and Supplementary Fig. 1). Using annual mean AIW transport estimates from our moored records as a reference in combination with the estimates of the long-term change in AIW height, we estimate that the overturning may have increased by 141% from the earlier to the later period, leading to a considerably shorter residence time (Supplementary Methods 3). Since the AIW transport correlates 92% with the heat to melt ice at the glacier base, an increased heat

supply (and thus enhanced submarine melting) can be expected for the recent period 2013–2017 in comparison with the earlier periods for which data are available. However, it is outside the scope of this study to provide direct quantitative estimates in melt rates based on AIW height variations on the continental shelf.

Our measurements provide several new insights to the bathymetric–oceanic control of heat supply below the 79NG and similar glacier–ocean systems illustrated by the schematic sketch in Fig. 4. It is widely accepted that the temperature of water interacting with marine-terminating glaciers is controlled by sill depth. Here, we provide observationally supported evidence that hydraulic control constrains the volume inflow of waters from the continental shelf into an ice shelf cavity (in our case below the 79NG). Due to the local topographic control, any changes in the AIW thickness and density upstream of the sill due to large-scale hydrographic variations determine the heat flux below the glacier tongue. We posit that bathymetric control of AIW transport towards the 79NG has limited the oceanic heat available for submarine melting, thereby sustaining the largest floating ice tongue in Greenland.

Our ocean measurements in the direct vicinity of ZI point to a similar topographic control of the ocean heat supply (Supplementary Discussion 2, Supplementary Methods 4 and Supplementary Fig. 2). While hydraulically controlled exchange flows for ice-shelf cavities have not been measured before, they have been investigated through a recent modelling study[31]. A better understanding of AIW variability on the continental shelf will be critical to predict future changes in
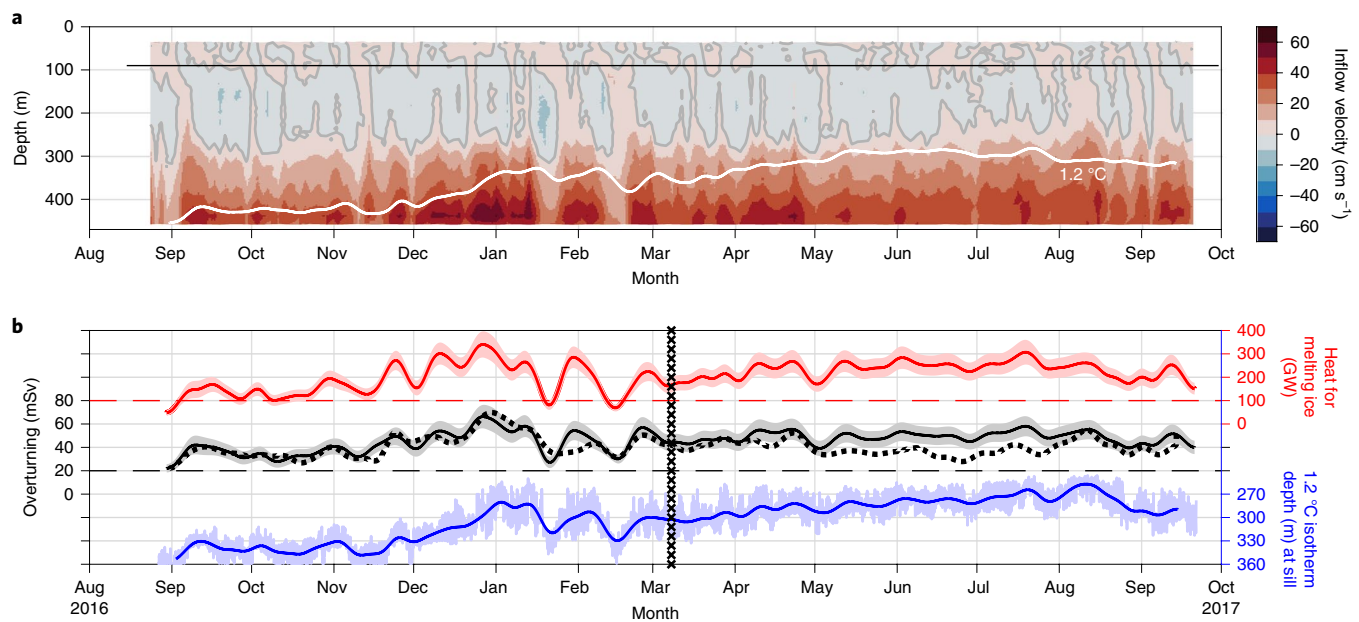
Fig. 3 | Temporal variability of the cavity overturning and of the heat for melting the underside of the 79NG. a, Time series of inflow/outflow velocities (red/blue) and 1.2 °C isotherm (white) based on moored velocity and temperature records taken at mooring site C. **b**, Time series of the heat going into melting the glacier from below (red); time series of the volume flux computed on the basis of the hydraulic control theory (dashed) compared with the computed overturning based on records from gateways A–D (black); time series of the depth of the 1.2 °C isotherm at mooring site E (blue). Error bars for heat and volume fluxes give systematic errors arising from the extrapolation methods (Methods). Error bars for isotherm displacements are time variations. Black markers in March highlight the date when the ADCP located in Dijmphna Sund stopped recording velocities.
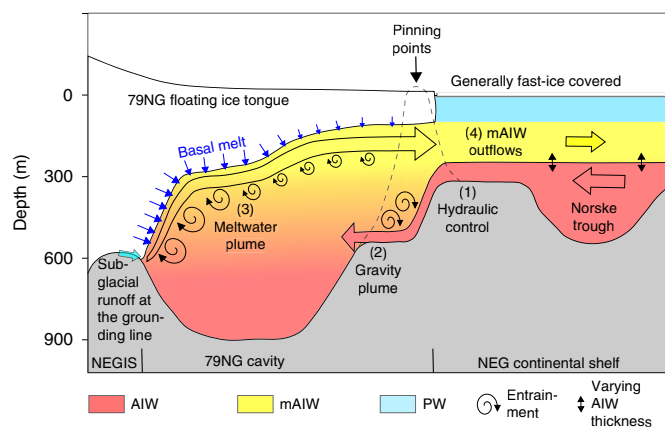
Fig. 4 | Sketch of the cavity circulation and water masses at the 79NG.
(1) Large-scale hydrographic variations, reflected by changes in the Atlantic water layer thickness, are subject to local topographic-sill (hydraulic) control. (2) Downstream of a sill, a descending gravity plume transports heat into the cavity. (3) Inside the cavity, the heat is used to melt the glacier from below. A positively buoyant meltwater plume causes turbulent mixing of AIW with glacial meltwaters, thereby probably intensifying the heat flux to the ice. (4) The heat lost due to glacial melting results in an export of glacially modified waters (mAIW) that are 0.9 °C cooler than the inflowing Atlantic waters. PW, polar water.

the ocean heat supply and submarine melt at the outlet glaciers of the NEGIS. In particular, the relevance of shelf wind fields[32] that were shown to drive winter-enhanced heat fluxes across continental shelves towards other Greenlandic glacial fjords[33,34] needs to be investigated. For the continental shelf offshore of the 79NG, a recent study shows that energetic topographic Rossby waves (at periods shorter than one month) propagate along the inflow

pathway of AIW from the shelf edge towards the 79NG[24]. We posit that such wave processes may have the potential of modulating the AIW transports into the cavity by displacing the AIW interface and thus hydraulic control.

Our improved understanding of the topographic control on ocean heat supply at the outlet glaciers of the NEGIS provides important ingredients for more realistic future ice sheet–ocean model projections. We pose that up-to-date model simulations of the past/future grounding-line retreat of 79NG and ZI[18,35] are undermined by a lack of detailed understanding of the ocean forcing. We conclude that to determine the future glacier stability and mass flux from the Greenland ice sheet contributing to sea-level rise, high-resolution coastal ocean bathymetry datasets are required together with near-coastal observations of hydrography and circulation.

Online content

Any methods, additional references, Nature Research reporting summaries, source data, extended data, supplementary information, acknowledgements, peer review information; details of author contributions and competing interests; and statements of data and code availability are available at https://doi.org/10.1038/s41561-019-0529-x.

References

1. Shephard, A. et al. A reconciled estimate of ice-sheet mass balance. *Science* **338**, 1183–1189 (2012).
2. Rietbroek, R., Brunnabend, S.-E., Jusche, J., Schröter, J. & Dahle, C. Revisiting the contemporary sea-level budget on global and regional scales. *Proc. Natl Acad. Sci. USA* **113**, 1504–1509 (2016).
3. Bamber, J. L. et al. The land ice contribution to sea level during the satellite era. *Environ. Res. Let.* **13**, 063008 (2018).
4. Aschwanden, A. et al. Contribution of the Greenland ice sheet to sea level over the next millenium. *Sci. Adv.* **5**, eaav9396 (2019).

5. von den Broeke, M. et al. Partitioning recent greenland mass loss. *Science* **326**, 984–986 (2009).
6. Sasgen, I. et al. Timing and origin of recent regional ice-mass loss in Greenland. *Earth Planet. Sci. Lett.* **333–334**, 293–303 (2012).
7. Enderlin, E. M. et al. An improved mass budget for the Greenland ice sheet. *Geophys. Res. Lett.* **41**, 866–872 (2014).
8. Kjeldsen, K. K. et al. Spatial and temporal distribution of mass loss from the Greenland ice sheet since AD 1900. *Nature* **528**, 396–400 (2015).
9. Holland, D. M., Thomas, R. H., de Young, B., Ribergaard, M. H. & Lyberth, B. Acceleration of Jakobshavn Isbrae triggered by warm subsurface ocean waters. *Nat. Geosci.* **1**, 659–664 (2008).
10. Thomas, R., Frederick, E., Krabill, E., Manizade, S. & Martin, C. Recent changes on Greenland outlet glaciers. *J. Glaciol.* **55**, 147–162 (2009).
11. Nick, F. M., Vieli, A., Howat, I. M. & Joughin, I. Large-scale changes in Greenland outlet glacier dynamics triggered at the terminus. *Nat. Geosci.* **2**, 110–114 (2009).
12. Seale, A., Christoffersen, P., Mugford, R. I. & O'Leary, M. Ocean forcing of the Greenland ice sheet: calving fronts and patterns of retreat identified by automatic satellite monitoring of eastern outlet glaciers. *J. Geophys. Res. Earth* **116**, F03013 (2011).
13. Straneo, F. et al. Impact of fjord dynamics and glacial runoff on the circulation near Helheim Glacier. *Nat. Geosci.* **4**, 322–327 (2011).
14. Straneo, F. & Heimbach, P. North Atlantic warming and the retreat of Greenland's outlet glaciers. *Nature* **504**, 36–43 (2013).
15. Rignot, E. & Mouginot, J. Ice flow in Greenland for the International Polar Year 2008–2009. *Geophys. Res. Lett.* **39**, L11501 (2012).
16. Mouginot, J. et al. Fast retreat of Zachariæ Isstrøm, northeast Greenland. *Science* **350**, 1357–1361 (2015).
17. Khan, S. A. et al. Sustained mass loss of the Northeast Greenland ice sheet triggered by regional warming. *Nat. Clim. Change* **4**, 292–299 (2014).
18. Choi, Y., Morlighem, M., Rignot, E., Mouginot, J. & Wood, M. Modeling the response of Nioghalvfjerdsfjorden and Zachari' Isstrom glaciers, Greenland, to ocean forcing over the next century. *Geophys. Res. Lett.* **44**, 11071–11079 (2017).
19. Mayer, C. et al. Large ice loss variability at Nioghalvfjerdsfjorden Glacier, Northeast-Greenland. *Nat. Commun* **9**, 2768 (2018).
20. Wilson, N., Straneo, F. & Heimbach, P. Satellite-derived submarine melt rates and mass balance (2011–2015) for Greenland's largest remaining ice tongues. *Cryosphere* **11**, 2773–2782 (2017).
21. Gagliardini, O., Durand, G., Zwinger, T., Hindmarsh, R. C. A. & Le Meur, E. Coupling of ice-shelf melting and buttressing is a key process in ice-sheets dynamics. *Geophys. Res. Lett.* **37**, L14501 (2010).
22. Sneed, W. A. & Hamilton, G. S. Recent changes in the Norske Øer Ice Barrier, coastal Northeast Greenland. *Ann. Glaciol.* **57**, 47–55 (2016).
23. Bourke, R. H., Newton, J. L., Paquette, R. G. & Tunnicliffe, M. D. Circulation and water masses of the East Greenland shelf. *J. Geophys. Res. Oceans* **92**, 6729–2740 (1987).
24. Münchow, A., Schaffer, J., and Kanzow, T. Ocean circulation connecting Fram Strait to glaciers off North-east Greenland: mean flows, topographic Rossby waves, and their forcing. *J. Phys. Oceanogr.* (in the press).
25. Mayer, C. et al. The subglacial cavity and implied dynamics under Nioghalvfjerdsfjorden Glacier, NE-Greenland. *Geophys. Res. Lett.* **27**, 2289–2292 (2000).
26. Straneo, F. et al. Characteristics of ocean waters reaching Greenland's glaciers. *Ann. Glaciol.* **53**, 202–210 (2012).
27. Wilson, N. J. & Straneo, F. Water exchange between the continental shelf and cavity beneath Nioghalvfjerdsbræ (79 North Glacier). *Geophys. Res. Lett.* **42**, 7648–7654 (2015).
28. Schaffer, J. et al. Warm water pathways toward Nioghalvfjerdsfjorden Glacier, Northeast Greenland. *J. Geophys. Res. Oceans* **122**, 4004–4020 (2017).
29. Arndt, J. E. et al. A new bathymetry of the Northeast Greenland continental shelf: constraints on glacial and other processes. *Geochem. Geophys. Geosyst.* **16**, 3733–3753 (2015).
30. Holland, P. R. The transient response of ice shelf melting to ocean change. *J. Phys. Oceanogr.* **47**, 2101–2114 (2017).
31. Zhao, K. X., Stewart, A. L. & McWilliams, J. C. Sill-Influenced exchange flows in ice shelf cavities. *J. Phys. Oceanogr.* **49**, 163–191 (2019).
32. Turton, J. V., Mölg, T. & Van As, D. Atmospheric processes and climatological characteristics of the 79N Glacier (Northeast Greenland). *Mon. Weather Rev.* **147**, 1375–1394 (2019).
33. Jackson, R. H., Straneo, F. & Sutherland, D. A. Externally forced fluctuations in ocean temperature at Greenland glaciers in non-summer months. *Nat. Geosci.* **7**, 503–508 (2014).
34. Fraser, N. J., Inall, M. E., Magaldi, M. G., Haine, T. W. N. & Jones, S. C. Wintertime fjord–shelf interaction and ice sheet melting in Southeast Greenland. *J. Geophys. Res. Oceans* **123**, 9156–9177 (2018).
35. Tabone, I., Robinson, A., Alvarez-Solas, J. & Montoya, M. Submarine melt as a potential trigger of the North East Greenland Ice Stream margin retreat during Marine Isotope Stage 3. *Cryosphere* **13**, 1911–1923 (2019).

Methods

Bathymetric data. Bathymetric data are rare around the coast of Greenland, while detailed knowledge of the seafloor is essential to understand the ocean heat transport within glacial fjords. During R/V *Polarstern*[36] expeditions PS100 and PS109, the hull-mounted Teledyne RESON Hydrosweep DS3 multibeam echo-sounding system was used to collect bathymetric data along the ship's track. The operating frequencies were between 13.6 and 16.4 kHz. Sound velocity profiles from hydrographic measurements were used to calibrate the bathymetric data, which were processed and cleaned in CARIS HIPS and SIPS. Finally, the data have been included in an update of the digital bathymetric model for the Northeast Greenland continental shelf[29] and subsequently incorporated into the global RTopo-2 dataset[37]. Bathymetric profiles along conductivity–temperature–depth (CTD)/lowered ADCP (LADCP) sections (Fig. 2a,c) were interpolated from the updated RTopo-2 dataset.

Hydrographic and velocity profiles. For our analysis, we use 18 hydrographic/velocity profiles carried out in summers 2016 and 2017 with R/V *Polarstern*[36] offshore the calving front of the 79NG. Ship-lowered CTD casts were carried out with a standard CTD SBE911plus system sampling at 24 Hz. We used water samples from Niskin bottles to calibrate conductivity sensors (salinity bottle–sensor deviation of 0.002 r.m.s.). All profiles were interpolated to a 1 dbar vertical resolution.

Two 300 kHz RDI Workhorse ADCPs (one upward and one downward oriented) were mounted on the frame of the CTD rosette to infer profiles of current velocities. Data were processed with the LDEO IX LADCP package, based on an inverse method[38] and constrained by the vessel-mounted ADCP, with a vertical resolution of 10 m and an accuracy of 4 cm s⁻¹. Cavity in-/outflowing waters along the calving front are defined as west-/eastward velocities (Fig. 2a), respectively. Current directions (including tides) in the CTD/LADCP section across the sill (Fig. 2c) were rotated into the along-flow direction following the shape of the bathymetry.

To cover the cavity in-/outflow, we assess the shallowest, shortest CTD/LADCP sections in the north–south direction between the pinning point islands. Data have been extrapolated linearly in a horizontal direction along the CTD/LADCP sections.

Hydrography and velocity time series. Temporal evolutions of temperatures, salinities and current vectors were recorded at distinct depth levels with instruments moored at five mooring positions (Supplementary Table 1). Four moorings were located within the main cavity–shelf exchange gateways A, B, C, and D (Fig. 1d), and a fifth (referred to as mooring E) was at the sill located upstream of the main inflow. In the vertical, all velocity records covered the depth range from (at most) 18 m above the seafloor to the average depth of the glacier base at 90 m. We linearly interpolate ADCP velocities between the bin depths for every time step (Supplementary Table 1). We consider horizontal flow above the glacier base perpendicular to the calving front to be zero as it is blocked by the glacier base. On the basis of our mean velocity profiles from the moored records, we find velocities to decrease toward the seafloor. To extrapolate moored velocities down to the seafloor, we assumed the speed at the seafloor to equal half the speed at the deepest bin and interpolated linearly in between.

Cavity overturning and residence time. To assess the strength of the cavity overturning, we computed volume transports of in- and outflowing waters on the basis of the velocity fields that were horizontally extrapolated (as detailed in this section) and subsequently gridded. Volume transports were calculated from the gridded velocity fields at 5 m depth intervals by integrating horizontally (multiplying velocities with the width of the gateway) as shown in Fig. 2b. Assuming that the cross-sections cover the entire flow across the calving front, a precise compensation among the in- and outflow components is required (neglecting meltwater fluxes). We find that velocities decrease towards the sidewalls at gateways B and C where several LADCP profiles are available (Fig. 2a). To account for reduced velocities towards the sidewalls and to achieve a closed time–mean mass budget, we reduced the velocity data (at each depth level) to 20% at horizontal distances less than 500 m to each sidewall (resulting in a deficit of 0.02 Sv). To assess the systematic errors associated with the extrapolation[39], we repeat the calculations with 0% and 40% reduced velocities at 500 m distances and then compare the results from these cases. At every hourly time step, the mass budget is closed individually by adding a time-varying, spatially uniform velocity to the entire velocity field[40]. The cavity overturning is defined by the maximum in vertical cumulative transports (cumulative sum from the seafloor to the average depth of the glacier base). It has been calculated for all three cases (with changing sideways reduction of the flow).

The best estimate of volume transports is given for the period when sensors at all moorings recorded data (between 29 August 2016 and 08 March 2017). The ADCP at mooring position D located in Dijmphna Sund stopped recording in March 2017, while all the other devices recorded data until recovery in September 2017. Our best estimate cavity overturning (based on all mooring records) correlates with the overturning lacking volume fluxes via Dijmphna Sund with a correlation coefficient of 0.96. The mean cavity overturning is underestimated by 6 mSv when

neglecting Dijmphna Sund. To prolong the time series of cavity overturning until summer 2017, we applied a linear regression (regression coefficients $\alpha = 1.06$ and $\gamma = 0.004$ with $y(t) = \alpha t + \gamma$, where y is the estimated overturning at time step t). The mean of the resulting time series (three cases) is used as our best estimate of the cavity overturning, and we consider the corresponding standard deviation as a quantification of its systematic errors (Fig. 3b).

Assuming a closed mass budget, the average residence time of waters in the cavity can be approximated by dividing the cavity volume by the estimated time–mean cavity overturning. The cavity volume has been computed on the basis of the bathymetry and ice base topography provided by the RTopo-2[37] dataset, giving a cavity volume of $640 \pm 80 \, \text{km}^3$, where the error stems from uncertainties in the depth measurements.

Heat, salt and freshwater budgets for a subglacial cavity. To infer melt rates at the glacier base from our oceanic measurements, we need to consider the complete heat, salt and mass budgets[39] for a control volume V_c containing all liquid water in a subglacial cavity[41] (Supplementary Fig. 3). The boundaries of V_c are defined by the glacier base, the sidewalls and seafloor of the subglacial cavity and the cross-section at the seaward end of the cavity (A_x, that is, along the calving front; vertical dashed line in Supplementary Fig. 3). We assume that the water in the cavity is well mixed such that it can be represented by a single (θ, S), where θ is the potential temperature and S is the salinity.

Neglecting any temporal changes in the control volume, the mass budget for the subglacial cavity[39] is given by:

$$\int_{A_x} u \, dA + Q_R + Q_{MW} = 0 \tag{1}$$

The first term is the volume flux through the cross-section along the calving front (Q_x), where we consider u to be the velocity across A_x with positive velocities to be directed into the control volume. The sum of the second and the third terms describes the total freshwater discharged into the cavity (the volume fluxes of subglacial runoff, Q_R, and basal meltwater, Q_{MW}).

The heat budget for the control volume[39] is given by:

$$\rho_0 c_P \int_{A_x} u \, \theta \, dA + \rho_0 c_P Q_R \theta_R + \rho_0 c_P Q_{MW} \theta_{MW} = \rho_0 c_P \int_{V_c} \frac{\partial \theta}{\partial t} \, dV + \rho_0 Q_{MW} L_{adj} \tag{2}$$

The terms on the left side of equation (2) are the advective heat fluxes through all boundaries: the heat transports across A_x (term 1; H_x in Supplementary Fig. 3), from subglacial runoff (term 2; H_R in Supplementary Fig. 3) and from basal melting (term 3; H_{MW} in Supplementary Fig. 3). The advective heat fluxes are balanced by changes in the ocean heat content (term 1 on the right side of equation (2); $H_{storage}$ in Supplementary Fig. 3) and the total heat extracted from the ocean to warm and/or melt ice (term 2 on the right side of equation (2); $H_{melting}$ in Supplementary Fig. 3). Constants ρ_0 and c_P are the density and heat capacity of seawater, respectively. θ_R and θ_{MW} are the potential temperatures corresponding to the in situ freezing temperatures at which the subglacial runoff and basal meltwater enter the control volume, respectively. The adjusted latent heat[39] (L_{adj}) is given by:

$$L_{adj} = c_i(\theta_{MW} - \theta_i) + L \tag{3}$$

which includes the heat required to raise the ice temperature to the melting point (considering the heat capacity of ice, c_i, and the ice temperature, θ_i) and the latent heat to melt ice (L).

The salt budget is given by the advective salt transport (F_x) through the cross-section A_x, which is balanced by the salt storage ($F_{storage}$) (ref. [39]):

$$\int_{A_x} u \, S \, dA = \int_{V_c} \frac{\partial S}{\partial t} \, dV \tag{4}$$

Advective heat and salt fluxes from moored records. We used our moored records to calculate advective heat and salt fluxes across the calving front section. Temperature and salinity time series were obtained by 5 and 11 recorders placed at different depths for moorings A and C, respectively, and slightly above the seafloor at moorings B and D. We developed extrapolation methods to grid temperature and salinity fields that are representative for each gateway at every point in time. CTD profiles taken in 2016 and 2017 at the different mooring locations (smoothed and averaged) were used to extrapolate θ/S data in the vertical (that is, from the uppermost moored instrument upward to the glacier base) to estimate complete θ/S profiles at every point in time. For moorings containing data loggers at different depths, the profiles between sensors were linearly extrapolated. Between the bottom-most sensor and the seafloor, data were extrapolated by assuming a constant value equal to the deepest θ/S record (justified by the assumption that bottom water was well mixed and sensors were located <14 m above the seafloor, Supplementary Table 1).

We assume that the largest errors of our extrapolated θ/S fields arise from the extrapolation between the uppermost sensor and the glacier base (that is, between 90 m and ~200 m, as it passes through the θ/S gradient between polar waters and

mAIW; Fig. 2b). To account for these errors when computing salt/heat fluxes, we estimated the mean deviation of θ/S profiles (measured in 2016 and 2017) from the θ/S profile predicted by our extrapolation method. In addition to our best estimate $\theta_{be}(h,t)$, with h being the height above the uppermost sensor, we constructed two error cases (θ_+/S_+, θ_-/S_-) for each gateway:

$$\theta_{+/-}(h,t) = \theta_{be}(h,t) \pm \frac{h - h_{\text{sensor}}}{h_{\text{glacierbase}} - h_{\text{sensor}}} d\theta \qquad (5)$$

Here $d\theta$ is an estimate for the temperature extrapolation error at the glacier base (equal to the mean deviation from the predicted value). This error is assumed to increase linearly from zero at the depth of the uppermost sensor to $d\theta$ at the glacier base (equation (5)). The same was done for salinity. The θ/S data were interpolated horizontally by assuming a constant value at every depth within each gateway.

To compute time series of the advective heat and salt fluxes, we combined each of the three cases of the velocity field with each of the nine cases of the θ/S field and used constants $\rho_0 = 1,027 \text{ kg m}^{-3}$ and $c_p = 3.986 \text{ kg kJ}^{-1}\text{K}^{-1}$. The means of those 27 cases at each time step are our best estimate for the heat and salt fluxes, and the standard deviations are estimates of their extrapolation errors.

Filter, time-mean and error estimates. We filtered the volume, advective heat and salt flux time series (and all related time series discussed below) with a lowpass filter using a Hann window of two weeks. The cutoff period has been chosen to still resolve the effects of topographic Rossby waves that are shown to be relevant for propagation of energy towards the coast with the peak energy in the shelf circulation at 20 d periods[24]. Our best estimates yield $Q_x = 46 \pm 11 \text{ mSv}$, $H_x = 214 \pm 63 \text{ GW}$ and $F_x = 2.4 \pm 0.6 \text{ kg s}^{-1}$. Means represent time means of our best estimate time series. Errors are estimated from the sum of systematic and statistical errors. Systematic errors are calculated on the basis of the time mean of the standard deviations arising from extrapolation errors. Statistical errors, that is, the standard error of the time mean, σ_m, were calculated by $\sigma_m = \frac{\sigma}{\sqrt{N-1}}$, where σ is the standard deviation of our best estimate flux time series and N represents degrees of freedom (quantified by the zero-crossing of the autocorrelation function of the time series).

Heat and salt storage from moored records. We estimate the heat and salt storage terms[39] (equations (2) and (4)) on the basis of the assumption that the variability at the calving front is representative of the variability over the entire control volume within the subglacial cavity. We assume the temperature/salinity time series to be the time- (14 d lowpass filtered) and volume-averaged temperature/salinity, which we approximated as the section-averaged temperature/salinity (for example, $S_0(t) = \int_{A_x} S(t)dA / \int_{A_x} dA$). We find the heat ($0.03 \pm 0.02 \text{ GW}$) and salt ($0.22 \pm 0.26 \text{ kg s}^{-1}$) storage terms to be small compared with the advective heat and salt fluxes.

Freshwater fluxes. The total freshwater flux can be calculated[39] on the basis of the advective salt flux, the salt storage and the section-averaged salinity:

$$Q_{\text{FW}} = \frac{1}{S_0}\left(F_x + F_{\text{storage}}\right) \qquad (6)$$

Furthermore, the total freshwater exported across the calving front is given by the sum of subglacial runoff and basal melt entering the cavity; that is, $Q_{\text{FW}} = Q_R + Q_{\text{MW}}$. Using the heat budget (equation (2)) and some transformations[39], the meltwater flux can be calculated by:

$$Q_{\text{MW}} = \frac{1}{\beta}\left[\rho_0 c_p Q_{\text{FW}}(\theta_R - \theta_0) + H_x - H_{\text{storage}}\right] \qquad (7)$$

with $\beta = \rho_0 L_{\text{adj}} - \rho_0 c_p(\theta_{\text{MW}} - \theta_R)$. We defined the temperature of basal meltwater to be the potential temperature corresponding to the mean in situ freezing temperature between 90 and 600 m depth (that is, the depth range of the glacier base) with a salinity ranging between 30 and 35 parts per thousand (ppt); that is, $\theta_{\text{MW}} = -2.05 \pm 0.14 \,^\circ\text{C}$. Accordingly, the runoff temperature, $\theta_R = -0.22 \pm 0.13 \,^\circ\text{C}$, was defined as the in situ freezing point of freshwater between 0 and 600 m. To compute L_{adj} (equation (3)), we use the heat capacity of ice of $c_i = 3.986 \text{ kg kJ}^{-1}\text{K}^{-1}$ and assume the ice temperature to be $\theta_i = -15 \pm 1 \,^\circ\text{C}$.

Heat to melt ice and basal melt rates. On the basis of the time series of the meltwater flux, we determine the heat going into melting the glacier from below (equations (2) and (3)). For our observation period, the total heat extracted from the ocean to warm and/or melt ice yields $208 \pm 61 \text{ GW}$ (Fig. 3b). Basal melt rates (MR) can be estimated by $\text{MR} = Q_{\text{MW}}/A_{\text{base}}$, where $A_{\text{base}} = 1,700 \pm 70 \text{ km}^2$ is the approximate area of the glacier base estimated from RTopo-2[37].

Froude numbers. To assess whether the volume transport through the inflow channel is constrained by the geometry of the strait itself (hydraulic control[42]), we computed Froude numbers (F). Froude numbers ($F = u/\sqrt{g'h}$) describe the ratio of the mean flow velocity (u) and the speed of long gravity waves ($\sqrt{g'h}$, with the reduced gravity $g' = g\Delta\rho/\rho_0$ and the height of the water column h). We applied our

hydrographic measurements to a 2.5-layer system such that we defined the middle layer to be within the 27.65 and 27.82 kg m^{-3} isopycnals and the lower layer between the 27.82 kg m^{-3} isopycnal and the seafloor. The lower layer is considered to be representative for a well-mixed flow of AIW into the glacier cavity; that is, u is the depth-averaged velocity below the 27.82 kg m^{-3} isopycnal and h is the height above the seafloor of the 27.82 kg m^{-3} isopycnal. For deriving the reduced gravity, we take $\Delta\rho$ as the mean densities between the two layers. Froude numbers >1 are indicative of a supercritical flow regime in which the flow through a strait is sufficiently large that no information (waves) (for example, on the interface height) can be transferred from the cavity (downstream basin) to the continental shelf (upstream basin).

Volume transport based on hydraulic control theory. Following the assumption that the ocean flow is topographically controlled, we predict volume fluxes on the basis of the channel width (w_s), the reduced gravity, the depth of the sill and the bifurcation depth (z_{bif}) (ref. [43]). The latter is classically inferred from the depth where density profiles from the upstream and downstream basins start to increasingly deviate from each other with increasing depth[43] (as an approximate measure for the upper bound of the gravity plume). We use the same approach but apply it to temperature profiles from interpolated moored temperature fields for the following reasons. First, temperatures mainly determine densities of the AIW/mAIW in our study area. Second, temperature loggers placed in various depths resolved temperature gradients while sensors measuring salinities were placed only at the shallowest and deepest depths (Supplementary Table 1). Third, inferring salinities from temperatures introduces errors because of a nonlinear behaviour of salinities and temperatures in our study region.

Comparing CTD profiles from the upstream basin with profiles from mooring positions A and E suggests that hydrographic data from both sites approximately represent hydrographic conditions from the upstream basin (not shown), while data recorded at mooring site C represent downstream conditions (Fig. 1d), used to calculate the bifurcation depth.

The difference of the sill depth and the bifurcation depth yields the reservoir height at the sill (h_{sill}). The Rossby radius of deformation ($L_d = \sqrt{g'h_{\text{sill}}}/f = 2.7 \text{ km}$) is slightly larger than the width of the strait (1.5 km/2.5 km at 300 m/200 m, respectively). Thus, rotation may become important but is neglected here. In the zero-potential vorticity limit[43] and for non-rotating cases, the maximum volume flux through a strait can be predicted by:

$$Q = \left(\frac{2}{3}\right)^{3/2} w_s(g')^{1/2}(h_{\text{sill}})^{3/2} \qquad (8)$$

We approximate the width of the strait w_s as a linear function of the bifurcation depth by $w_s \cong -10 \times (z_{\text{bif}} - 450 \text{ m})$ (based on the strait widths at 200 and 300 m given above). On the basis of densities extrapolated from moorings A (upstream) and B (downstream), we compute a reduced gravity of:

$$g' = g \frac{\rho_{\text{upstream}}(z_{\text{sill}}) - \rho_{\text{downstream}}(z_{\text{sill}})}{\rho_0} \qquad (9)$$

with $g = 9.81 \text{ m s}^{-2}$, $z_{\text{sill}} = 325 \text{ m}$ and $\rho_0 = 1,027.8 \text{ kg m}^{-3}$. Over time, the reduced gravity does not vary much, whereas temporal changes in w_s and h_{sill} are large.

Data availability
Processed CTD data from 2016 (https://doi.org/10.1594/PANGAEA.871025) and 2017 (https://doi.org/10.1594/PANGAEA.885358) are available at the World Data Center PANGAEA. CTD raw data files from 2016 and 2017 are available at https://doi.org/10.1594/PANGAEA.871701 and https://doi.org/10.1594/PANGAEA.883366. Raw LADCP data are available at https://doi.org/10.1594/PANGAEA.870995 for 2016; data from 2017 are available at https://doi.org/10.1594/PANGAEA.904021. Raw mooring data are available at https://doi.pangaea.de/10.1594/PANGAEA.904023 (for mooring recoveries in 2017) and at https://doi.org/10.1594/PANGAEA.904022 (for mooring recoveries in 2018). Processed mooring data are found at the World Data Center PANGAEA under https://doi.org/10.1594/PANGAEA.909471 together with a report on data processing (Schaffer, Janin (2019): Report on Mooring processing of PS109/PS114 recoveries (NE Greenland continental shelf), 9 pp, hdl:10013/epic.4cf66b0e-b6c2-4e0c-aef1-a709c493c1dc). Temperature profiles in front of ZI taken in 2016 are available at https://doi.org/10.1594/PANGAEA.870997; 2017 data are available at https://doi.org/10.1594/PANGAEA.904016. A collection of historic and recent CTD profiles carried out on the Northeast Greenland continental shelf[24] are available from J.S. (janin.schaffer@awi.de) on request. The full-resolution bathymetry data from multibeam echo soundings in front of the 79NG are available from D.H.R. (d.h.roberts@durham.ac.uk) on request. The interpolated bathymetry grid for Northeast Greenland with a 250 m grid resolution that includes multibeam echo-sounding data collected in 2016 in front of 79NG and depth information collected close to ZI is available at https://doi.org/10.1594/PANGAEA.909628. Maps based on the updated RTopo-2 dataset are available at https://doi.org/10.1594/PANGAEA.905295. Satellite images recorded by Landsat 8 on 28 April 2016 (Fig. 1c,d) and 7 September 2016 (Supplementary Fig. 2) can be downloaded from Earth Explorer (https://earthexplorer.usgs.gov/) courtesy of the US

Geological Survey. Ice velocities based on 'Greenland ice velocity map 2017/2018 from Sentinel-1 [version 1.0]' and the grounding-line position derived from ERS-1/-2 SAR and Sentinel-1 SAR interferometry are available from ENVEO within the ESA Initiative Greenland Ice Sheet CCI (https://esa-icesheets-greenland-cci.org/).

Code availability
MATLAB routines used for data processing and analysis are available from the corresponding author on request.

References

36. Alfred-Wegener-Institut Helmholtz-Zentrum für Polar- und Meeresforschung & Knust, R. Polar Research and Supply Vessel POLARSTERN Operated by the Alfred-Wegener-Institute. *J. Large-Scale Res. Facilities* **3**, A119 (2017).
37. Schaffer, J. et al. A global, high-resolution data set of ice sheet topography, cavity geometry, and ocean bathymetry. *Earth Syst. Sci. Data* **8**, 543–557 (2016).
38. Visbeck, M. Deep velocity profiling using lowered acoustic Doppler current profilers: bottom track and inverse solutions. *J. Atmos. Ocean. Technol.* **19**, 794–807 (2011).
39. Jackson, R. H. & Straneo, F. Heat, salt, and freshwater budgets for a glacial Fjord in Greenland. *J. Phys. Oceanogr.* **46**, 2735–2768 (2016).
40. Kanzow, T. et al. Observed flow compensation associated with the MOC at 26.5° N in the Atlantic. *Science* **312**, 938–941 (2007).
41. Schaffer, J. *Ocean Impact on the 79 North Glacier, Northeast Greenland*. PhD Thesis, Univ. Bremen (2018).
42. Pratt, L. J. Recent progress on understanding the effects of rotation in models of sea straits. *Deep Sea Res. Part II Top. Stud. Oceanogr.* **51**, 351–369 (2004).
43. Whitehead, J. A. Topographic control of oceanic flows in deep passages and straits. *Rev. Geophys.* **36**, 423–440 (1998).

Author contributions
J.S., T.K. and W.-J.v.A. conceived the study; J.S., T.K., W.-J.v.A. and L.v.A. participated in the collection of oceanographic data; J.S. and W.-J.v.A. processed the mooring data; L.v.A. and W.-J.v.A. processed LADCP data; D.H.R. collected the bathymetric data; J.E.A. processed bathymetric data; J.S. was responsible for data analysis and J.S., T.K. and W.-J.v.A. interpreted the data. J.S. wrote the manuscript and all authors commented at all stages.

Competing interests
The authors declare no competing interests.

Additional information
Supplementary information is available for this paper at https://doi.org/10.1038/s41561-019-0529-x.

Correspondence and requests for materials should be addressed to J.S.

Peer review information Primary handling editor: Heike Langenberg.

Reprints and permissions information is available at www.nature.com/reprints.